JOURNAL OF SPACECRAFT AND ROCKETS
Vol. 41, No. 5, September–October 2004

Experimental Expansion Tube Study of the Flow over a Toroidal Ballute

T. J. McIntyre,* I. Lourel,† T. N. Eichmann,‡ R. G. Morgan,§ P. A. Jacobs,¶ and A. I. Bishop**
University of Queensland, Brisbane, Queensland 4072, Australia

An experimental investigation of high-enthalpy flow over a toroidal ballute (balloon/parachute) was conducted in an expansion tube facility. The ballute, proposed for use in a number of future aerocapture missions, involves the deployment of a large toroidal-shaped inflatable parachute behind a space vehicle to generate drag on passing through a planetary atmosphere, thus, placing the spacecraft in orbit. A configuration consisting of a spherical spacecraft, followed by a toroid, was tested in a superorbital facility. Measurements at moderate-enthalpy conditions (15–20 MJ/kg) in nitrogen and carbon dioxide showed peak heat transfer rates of around 20 MW/m^2 on the toroid. At higher enthalpies (>50 MJ/kg) in nitrogen, carbon dioxide, and a hydrogen–neon mixture, heat transfer rates above 100 MW/m^2 were observed. Imaging using near-resonant holographic interferometry showed that the flows were steady except when the opening of the toroid was blocked.

Nomenclature

a = equilibrium sound speed, m · s^{-1}
C = constant
C_p = specific heat at constant pressure, J · kg^{-1} · K^{-1}
D = drag, N
d = spacecraft center-to-center offset from toroid, mm
h = specific enthalpy, J · kg^{-1}
K = stagnation point streamwise velocity gradient, s^{-1}
L = characteristic length scale, m
M = Mach number
m = order of truncation error in computational fluid dynamics (CFD) code
N = number of cells in the simulation
Pr = Prandtl number
p = pressure, Pa
$\dot{Q}$ = total heat flux, W
$\dot{q}$ = heat flux, Wm^{-2}
Re = Reynolds number based on freestream properties and U_{eq}
Re_e = Reynolds number based on postshock properties and U_{eq}
r = toroid cylinder radius, 3 mm
St = Stanton number based on freestream conditions
St_e = Stanton number based on postshock density using U_{eq} as the velocity
T = temperature, K
U = velocity, m · s^{-1}
U_{eq} = equivalent flight speed $\sqrt{(2 \times \text{stagnation enthalpy})}$, m · s^{-1}
γ = specific heat ratio
Δx = length of a cell within the grid of the CFD code
μ = viscosity (Pa · s)
ρ = density, kg · m^{-3}

Subscripts and Superscripts

e = ballute stagnation conditions
eq = equivalent flight conditions
w = wall conditions
0 = isentropic total conditions
1 = initial (fill) value
2 = postprimary shock value
∞ = freestream in test section

Introduction

AEROCAPTURE is the process in which an interplanetary vehicle acquires sufficient drag for orbit insertion in a single pass through a planet's atmosphere. This process requires that the vehicle enter into the lower altitudes, where the atmospheric density, and, therefore, the drag generated, is sufficiently large. Significant heat loading can result, and this necessitates the development of suitable heat shields, the design being dependent on the entry speed and type of atmosphere. Current aerocapture studies focus on two approaches, the use of the aeroshell and the ballute. In the former, the drag is generated by a forward-facing ablative heat shield on the vehicle. The latter approach involves the deployment of a large towed balloon/parachute assembly that generates equivalent drag at lower densities and, thus, indirectly reduces the heat load on the vehicle.[1,2]

To see the effect of length scale, consider the drag D on a hypersonic vehicle. The drag is proportional to the area of the vehicle, the square of the vehicle's velocity and the atmospheric density, that is, $D \propto \rho U^2 L^2$, where L is the characteristic length scale of the vehicle. At any given velocity on a reentry path, the required drag will be set by the payload requirements and mission objectives. To achieve this drag, the altitude must be set to give the appropriate density for the velocity by the relation

$$\rho \propto (D/U^2 L^2) \tag{1}$$

However, the associated local heat flux, $\dot{q}$ scales as

$$\dot{q} \propto (\sqrt{\rho} U^3/\sqrt{L}) \propto \left(U^2 \sqrt{D} \big/ L^{\frac{3}{2}}\right) \tag{2}$$

There is evidently a significant reduction in local heating rate to be gained by using large length scales on the drag surfaces. The total heat transfer will scale with the exposed surface area:

$$\dot{Q} \propto \dot{q} L^2 \propto U^2 \sqrt{DL} \tag{3}$$

Received 18 July 2002; revision received 1 November 2003; accepted for publication 1 November 2003.

*Senior Research Fellow, Centre for Hypersonics, Department of Physics; mcintyre@physics.uq.edu.au.

†Graduate Student, Centre for Hypersonics, Department of Mechanical Engineering.

‡Graduate Student, Centre for Hypersonics, Department of Physics.

§Professor, Centre for Hypersonics, Department of Mechanical Engineering. Associate Fellow AIAA.

¶Senior Lecturer, Centre for Hypersonics, Department of Mechanical Engineering.

**Postdoctoral Research Fellow, Department of Physics; currently Research Associate, Department of Physics, Heriot-Watt University, Edinburgh, Scotland EH14 4AS, United Kingdom.

and will actually increase in proportion to $\sqrt{L}$. However, because the local heat flux is reduced, the heat may be rejected from a nonablative surface, at relatively low T_w, giving a significant reduction in total heat-shield weight. For radiant cooling ($\propto T_w^4$), the required wall temperature will scale with

$$T_w \propto \left(U^2\sqrt{D}\big/L^{\frac{3}{2}}\right)^{\frac{1}{4}} \propto L^{-\frac{3}{8}} \tag{4}$$

Hence, an increase in length scale by a factor of 25 reduces the wall temperature by a factor of about 3. This change would be adequate to reduce T_w on the ballute from typical ablative values of around 2500 K to about 800 K, which could be sustained by modern plastics. Evidently, length scales on the order of hundreds of meters will be required to implement this concept in some atmospheres.

This paper details the experimental investigation of moderate- and high-enthalpy flow over a spacecraft trailed by a toroidal ballute and follows an earlier study that examined flows relevant to entry into the atmospheres of Mars, Titan, and Neptune.[3] The earlier study was conducted in a free-piston-driven reflected shock tunnel that generates a high-temperature, high-pressure, near-stagnant reservoir of test gas before expanding the gas to high freestream velocities via a steady expansion in a supersonic nozzle. The current study was performed using a superorbital expansion tube. It differs from a shock tunnel in that the freestream gas is accelerated using an unsteady expansion, without first stagnating the test gas. Significantly higher stagnation enthalpies can, thus, be achieved because the gas is not subject to the radiation losses and temperature limitations of the nozzle reservoir of a shock tunnel. The higher enthalpies allow for a more complete simulation of the planetary entry conditions including the chemical effects of dissociation and ionization. However, both the test time and core flow size are reduced in an expansion tube. In the experiments performed here, the test time was of the order of 50–100 μs, and the exit diameter of the flow was 85 mm, of which the core flow was measured to be 60 mm.

The experimental series covered five separate operating conditions (labeled A–E). Moderate-enthalpy (~20 MJ/kg) carbon dioxide and nitrogen measurements were performed for comparison with the earlier studies. To enter the regime where ionization and high levels of dissociation occur, high-enthalpy (~60 MJ/kg) carbon dioxide and nitrogen conditions were examined. Entry into the gas giants was simulated using a hydrogen–neon mixture. The use of neon in place of helium in the test gas allows ground-based measurements to be performed at lower freestream experimental enthalpies than the actual flight conditions.[4]

Two flow diagnostic techniques were used throughout these studies. A heat transfer gauge was used at the stagnation line of the ballute for each experiment. Shock shapes were imaged using near-resonant holographic interferometry.

Expansion Tube Facility

Expansion Tube Operation

The experiments were performed in the superorbital expansion tube, X2, shown in Fig. 1.[5,6] This free-piston-driven expansion tube has a total length of around 20 m with an internal diameter at the tube exit of 85 mm. The driver gas is compressed in a two-stage process by a compound piston launched using a double-diaphragm arrangement. Initial compression occurs in a 273-mm-diam tube at comparatively low pressures. Higher pressures are achieved after the heavier central part of the piston detaches and passes into a tube with a diameter of 91 mm, terminated by the primary diaphragm. Beyond this, the tube operates as a conventional expansion tube. The test gas is initially shock heated in the shock tube and then expanded unsteadily to the test condition through the acceleration tube.

Control of the freestream conditions was achieved by varying a number of parameters. For the high-enthalpy conditions, the driver gas consisted of pure helium. To achieve lower enthalpy conditions, a mixture of argon and helium was used to obtain a lower driver gas sound speed and, hence, a weaker shock in the shock tube. Fine tuning of the exit conditions was obtained by controlling the initial pressures in the shock tube and the accelerator tube. To obtain the very low densities required for the study, the fill pressures for the accelerator tube were of the order of 2 Pa, which approaches the limit of resolution of the pressure gauges of the facility. Some shot-to-shot variation was observed due to the uncertainties in the repeatability of this fill pressure.

Freestream Conditions

Moderate and high enthalpy freestream conditions relevant to planetary missions were generated in carbon dioxide and nitrogen test gases. Furthermore, a condition designed to simulate entry into the atmosphere of the gas giants was developed. Table 1 summarizes the nomenclature of the measurement sets and the operating conditions of the test flow for the study. In Table 1, the binary scaling parameter is based on the density behind an equilibrium normal shock formed in front of the ballute, ρ_e, and the radius of the toroid cross section, $r = 3$ mm. The equilibrium calculation is used for comparison with the previous study,[3] although significant nonequilibrium effects are expected in the shock layer around the toroid given the high enthalpy and low binary scaling parameter for these conditions. Details of the calculation of freestream conditions are given later.

Test times in the facility vary depending on the conditions used. For the shots performed here, it is estimated that the test time is 80 μs for conditions A and C and 30 μs for conditions B, D and E.

Model

Three models were built for the tests, and a new heat transfer gauge was installed for every run. Figure 2 shows the main ballute

Table 1 Freestream conditions

Condition	Gas	Enthalpy, MJ/kg	Binary scaling $\rho_e r$, kg/m^2	Mach number
A	CO_2	17–18	$(1.2\text{–}1.6) \times 10^{-4}$	7.7–8.3
B	CO_2	48–52	$(8\text{–}15) \times 10^{-5}$	9.3–10.3
C	N_2	17–19	$(6\text{–}8) \times 10^{-5}$	7.2–8.1
D	N_2	52–58	$(6\text{–}11) \times 10^{-5}$	8.1–9.0
E	H_2/Ne[a]	79–82	$(2\text{–}3) \times 10^{-5}$	8.2–8.7

[a] Mixture for condition E was 15% H_2, 85% Ne.

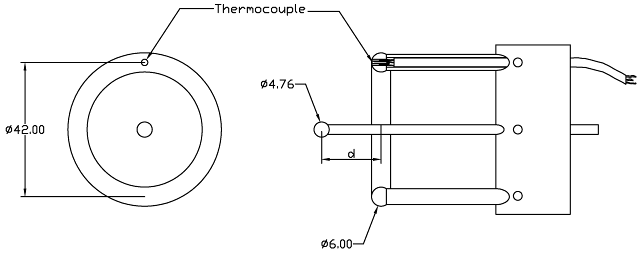

Fig. 2 Schematic diagram of the ballute and spacecraft model; all dimensions are in millimeters.

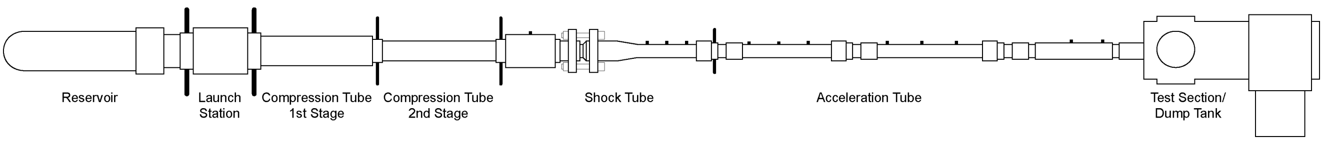

Fig. 1 Schematic diagram of the X2 expansion tube.

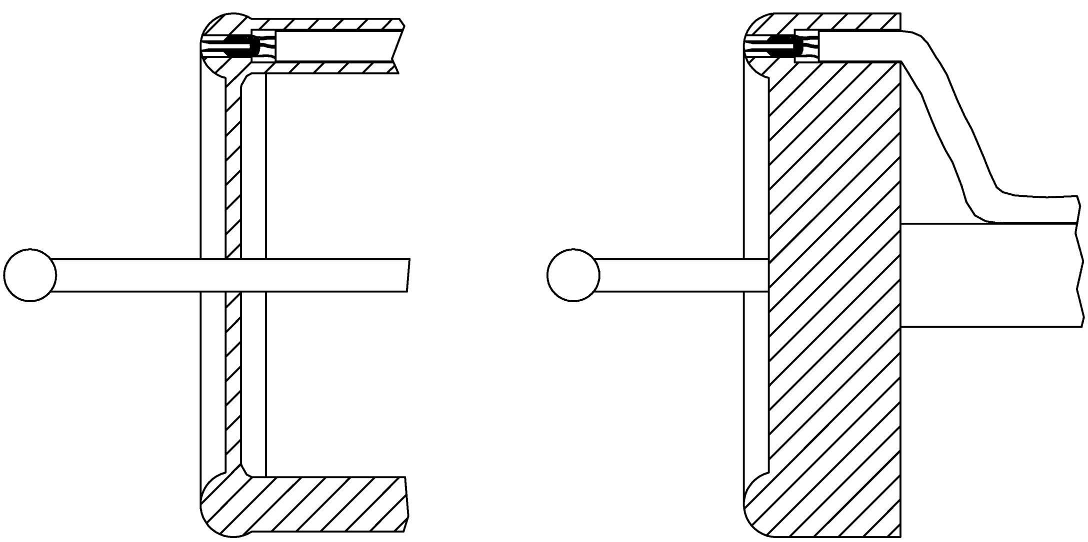

Fig. 3 Schematic diagram of the two blocked models: a) model used for conditions B and E and b) model used for conditions A, C, and D.

model used, which was scaled from the model used in the shock tunnel study.[3] A metal ring (42-mm overall centerline diameter and 6-mm cross-sectional diameter) was used to represent a rigid toroidal ballute, and a sphere (4.76 mm in diameter) mounted on a cylindrical rod was used to represent the leading spacecraft. The nominal value of the separation between the centers of the spacecraft and the ballute, d, was 18.6 mm, scaled from the previous study.[3]

Depending on the inner diameter of the toroid, it is possible for the flow through the toroid to become choked. To investigate such a phenomena, one experiment was conducted at each of the five test conditions. The choked situation was simulated by physically blocking the opening of the ballute ring. Initially, a stainless-steel plate was soldered to the ballute at the center of the opening (Fig. 3a). A hole located at the center of the plate allowed the sting of the spacecraft to go through and d remained unchanged from the nominal value. This model was used for the experiments at conditions B and E. A second equivalent model (Fig. 3b) was manufactured and used for conditions A, C, and D.

Estimation of Freestream Conditions

The flow conditions at the end of the acceleration tube are estimated from a mix of measurements and computational fluid dynamics (CFD) simulations. Properties that can be measured readily are the initial fill pressures and temperatures, the shock speeds, and the static pressures at a number of locations in both the shock tube and acceleration tube.

The calculations start with the postshock static pressure p_2 and initial fill temperature T_1 in the shock tube and the incident shock speed as measured by time-of-flight toward the end of the shock tube. A one-dimensional ideal flow model of the primary-shock compression process, with equilibrium chemistry assumed, is used to compute the remaining pre- and postshock conditions. Calculations for similar operating conditions using nonequilibrium chemistry in the one-dimensional analysis have produced the same estimates for the postprimary-shock flow properties as an equilibrium calculation (personal communication, B. Stewart, University of Queensland, 2003).

These postshock conditions in the shock tube are then used as an inflow boundary condition for an axisymmetric viscous flow simulation of the expansion process within the acceleration tube. This simulation is done with the MB_CNS code[7] and an equilibrium-chemistry look-up table generated with the CEA[8,9] code. MB_CNS performs a time integration of the Navier–Stokes equations for two-dimensional axisymmetric flow on a block-structured mesh. The integral form of the conservation equations is used, with the flowfield being recorded as cell-average values. An explicit time-stepping scheme is used to update the conserved quantities within each cell. Although the explicit update scheme is simple and readily parallelized, the restriction to small time steps required to satisfy the numerical stability limits became a problem for one of the flow conditions. The code has a shock-capturing capability that is provided by a limited reconstruction of the flowfield data using quadratic patches combined with an adaptive flux calculator that is suitable for flows with very strong shocks. This flux calculator switches between the equilibrium-flux method[10] (EFM) and the AUSMDV flux calculator,[11] with the more dissipative EFM being selected for cell interfaces that are near a shock.

At the start of the simulation, test gas with postshock conditions is placed at the upstream boundary and acceleration gas at low pressure fills the rest of the acceleration tube. The actual X2 facility was operated with a small amount of air in the acceleration tube at the start of the run. This gas provides a way of regulating the amount of expansion that the test gas experiences and, in the simulations, was modeled by an equivalent amount of the test gas. The numerical simulation of the unsteady expansion process through the acceleration tube allows the incident shock, contact surface, unsteady expansion, and tube-wall boundary layer all to develop implicitly within the flow. The final test flow parameters can then be extracted at the appropriate positions along the simulated acceleration tube.

Ideally, we would calculate the expanding flow with a nonequilibrium chemical model, but such a capability was not available. Our options included the use of a chemical equilibrium model or an assumption that the test-gas chemistry remains frozen at the state behind the primary shock. Experience with the X1 expansion tube facility[5] indicated that equilibrium chemistry calculations through the unsteady expansion gave flow estimates that were in reasonable agreement with experimental measurements, whereas frozen chemistry calculations did not. Equilibrium chemistry has been used for the calculations presented here.

Of the computed flow parameters, shock speed and static pressure can be checked against physically measured values. Take condition B, for example. Convergence of the numerical simulation was checked by running calculations with different resolutions and extrapolating to the limit of zero cell size. Computed estimates for the shock speed were assumed to differ from the true, that is, limiting value, by an error $C\Delta x^m$, where $\Delta x = 1/\sqrt{N}$ represents the length scale of a cell within the grid and the exponent m represents the order of truncation error for the CFD code. With sample simulations with $N = 38{,}000$, 44,850, 64,500, 88,896 and 175,500, and $m = 1.6$ assumed, the fitted value for the true shock speed is 9.363 ± 0.019 km/s. Taking $m = 1.3$ gives a limiting value of 9.371 ± 0.022 km/s. Both limiting values compare favourably with the experimentally measured value of 9.4 km/s. The nominal calculation with $N = 64{,}500$

had a shock speed within 0.5% of the limiting values. A similar extrapolation was done for the average static temperature during the test flow period, and the nominal calculations provided an estimate within 0.2% of the limiting value of 2680 K ($m = 1.6$).

Test Condition Variations

For each of the nominal test conditions (except the hydrogen–neon simulations), the flow conditions were calculated using the preceding method. However, within each set of conditions, shot-to-shot variations occurred in the secondary shock speed, which led to changes around the nominal flow properties.

The full axisymmetric simulation was not rerun for each shot to calculate the new properties, but a one-dimensional flow correction on the core flow properties was performed to allow for the effects of the experimentally measured differences. Noting that variations were due primarily to changes in the secondary shock speed, the influence on the exit flow was then due to changes in the truncation point of the unsteady expansion, a process that is primarily one dimensional. For small perturbations to this point, a one-dimensional correction was calculated using the local equilibrium gas conditions given by the CFD output.

For a change $\mathrm{d}U$ in the gas speed, the corresponding change in the sound speed, $\mathrm{d}a$, is given by

$$\mathrm{d}a = -\frac{(\gamma - 1)}{2}\mathrm{d}U \tag{5}$$

The resulting change in enthalpy, $\mathrm{d}h$, is given by

$$\mathrm{d}h = \frac{2a\mathrm{d}a}{\gamma - 1} = -a\mathrm{d}U = C_p\mathrm{d}T \tag{6}$$

The change in velocity allows the change in temperature to be estimated, and the corresponding change in pressure can be found from the isentropic relationship:

$$p_2/p_1 = (T_2/T_1)^{\gamma/(\gamma-1)} \tag{7}$$

These calculations are approximate because the gas properties change and γ and C_p are not fixed. However, when it is noted that the equilibrium unsteady expansion is isentropic, the real gas properties can be found at the calculated pressure using the entropy of the flow calculated by the CFD. This calculation was again performed using the CEA code.[8,9] When the self-consistent set of gas properties thus calculated are used, the true gas velocity U can be recalculated from Eq. (5). If this is significantly different from the experimental target value, iteration may be needed. There is still a small approximation inherent in using a fixed γ in Eq. (5) to find the velocity, which may be reduced by dividing the calculation up into a number of smaller steps. However, it was found that the changes in γ are small over the range of velocities covered in each set.

For the hydrogen–neon flows, the MB_CNS code required impractical times to solve because of the stability limit on the explicit time step, and a one-dimensional equilibrium analysis was used throughout. For this case, the unsteady expansion was assumed to start from the conditions calculated behind an equilibrium primary shock. The unsteady expansion was then split up into a number of isentropic pressure increments, and intermediate gas properties and velocities were calculated from the known entropy and pressure as outlined earlier. The velocity change across each increment was calculated from Eq. (6). The expansion was truncated for each run at the experimentally measured shock speed. For all of the runs, the secondary shock velocity was taken to be the final test gas speed at the tunnel exit. This assumption is used because the viscous effects in high-speed, low-density facilities cause the interface to catch up with the shock.[12]

Stagnation Point Heat Flux

The stagnation point heat flux was calculated for each test based on the calculated flow conditions. The reference length scale for the calculation of Reynolds numbers was taken to be the radius of the cylindrical section of the toroid, r. The expression for the stagnation point heat flux is[13]

$$\dot{q} = 0.57\mathrm{Pr}^{-0.6}\sqrt{\rho_e\mu_e K}\,(\rho_w\mu_w/\rho_e\mu_e)^{0.1}(h_e - h_w) \tag{8}$$

which applies for a two-dimensional cylinder, and is used as a first estimate for the toroid, which is a wrapped-around cylinder. The value of $(\rho_w\mu_w/\rho_e\mu_e)$ is taken to be 1.26, as used previously,[3] and the effect of wall enthalpy is ignored in comparison to the total enthalpy. Subscript e represents conditions at the edge of the boundary layer, which can here be substituted by the stagnation conditions.[3] K is the velocity gradient at the stagnation point and can be estimated using Newtonian theory as

$$K = U_\infty/2r\sqrt{8\rho_\infty/\rho_e} \tag{9}$$

In our analysis, the stagnation conditions behind the shock are taken to be the same as the ballute postshock static conditions. There is very little change in temperature and density in equilibrium flow at these high enthalpies because postshock kinetic energy is less than 1% of the total enthalpy for all conditions. In a separate calculation using MB_CNS, there was negligible difference between two-dimensional planar and axisymmetric calculations of K. There was, however, a shift of 0.08 mm toward the axis for the location of the stagnation point.

Reynolds and Stanton numbers are calculated from pre- and postshock conditions as

$$Re_\infty = \rho_\infty U_{\mathrm{eq}} r/\mu_\infty, \qquad Re_e = \rho_e U_{\mathrm{eq}} r/\mu_e \tag{10}$$

$$St_\infty = \dot{q}/\rho_\infty U_{\mathrm{eq}} h_0, \qquad St_e = \dot{q}/\rho_e U_{\mathrm{eq}} h_0 \tag{11}$$

Flow Instrumentation and Visualization

Heat Transfer

The model was instrumented with a fast-response (1 μs), in-house constructed, coaxial type-E thermocouple[14,15] at the stagnation point of the ballute ring as shown in Figs. 2–4. To achieve a fast-response time, it was necessary for the thermocouples to have very low thermal mass (minute junction depth). At 2 mm, the diameter of the thermocouples was significant compared to the diameter of the ballute cross section (6 mm), and therefore, it was necessary to round off the edges of the thermocouples to produce a continuous surface finish on the ballute ring. The thermocouple was generally replaced after each experiment due to the pitting of the surface and the degradation of the epoxy insulation.

To minimize electrical noise, the model was isolated from the tunnel. The use of shielded, low microphonic cables and a 200-kHz low-pass filter produced signals with very low-noise levels.

Digitization and recording of the data were performed with a single sample transient recorder manufactured in-house. A sampling rate of 4 MHz was used and 8 kB of data were recorded for each channel. The thermocouple signal was amplified by a factor of 500, and curve-fitted polynomials derived from standard EMF-temperature correlations[16] were validated and used to convert time-resolved

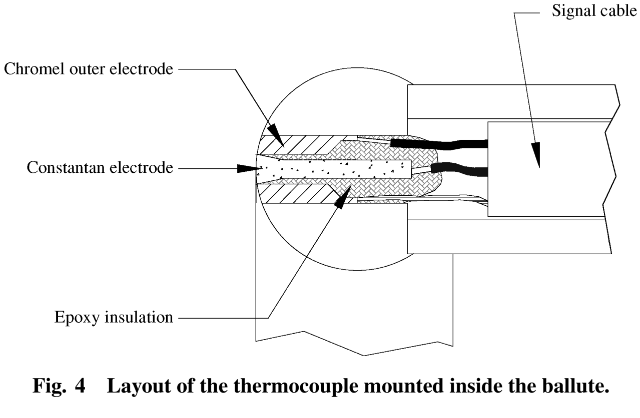

Fig. 4 Layout of the thermocouple mounted inside the ballute.

voltage to temperature rise data. Standard EMF-temperature correlations carry an uncertainty of around ±1.7% (Ref. 17), and this directly translates to a ±1.7% uncertainty in the final heat flux calculated.

The temperature signals were digitally processed to give surface heat flux using the semi-infinite one-dimensional heat-conduction model outlined by Schultz and Jones.[18] The epoxy insulating medium between the constantan and chromel thermoelements is assumed to have little influence on the overall thermal properties of the gauge, and therefore, the value of $\sqrt{(\rho c k)}$ required for the calculation of heat flux was taken to be the average value of the two thermoelements.[14] The actual value of $\sqrt{(\rho c k)}$ is expected to vary from gauge to gauge depending on the composition of the thermocouple junction. The temperature-dependent values of $\sqrt{(\rho c k)}_{\mathrm{constantan}}$ and $\sqrt{(\rho c k)}_{\mathrm{chromel}}$ are ±7% that of the average value, according to the thermal data published by Sundqvist.[19] This carries through directly to a ±7% uncertainty in heat flux.

A temperature rise of up to 200 K was measured in the test time. Variation of the thermoelectric properties with temperature has been taken into account in the derivation of heat flux. Whereas one can estimate and reduce the uncertainties associated with the thermoelectric properties, one cannot quantify the errors introduced physically. Inconsistent thermocouple junction depth or inappropriate mounting of the gauge will give rise to spurious measurements. Calibration of the individual thermocouple gauge in its final mounting position, however impractical, will serve to improve the repeatability in the heat flux measurements. All aspects of the thermocouple, including details on the thermal data and further error analysis, may be found in Lourel and Morgan.[14]

Near Resonant Holographic Interferometry

Holographic interferometry was used to obtain the flowfield images.[20] A coherent beam of light is passed through the test section in the absence of any flow and is recorded holographically. A second beam, generated during the period of established flow, is similarly recorded on top of the first. Subsequent reconstruction of these beams leads to the formation of an interferogram that can be analyzed to yield quantitative information about the variations in flow density. In the current application, the densities are very low, which renders standard interferometry insensitive to the flowfield. The fringe shift is, thus, enhanced by utilizing the increased refractivity present near an absorption line of a gas species present in the flow. When the laser output is tuned near the peak of the refractive index distribution,[21] it is possible to enhance the sensitivity by several orders of magnitude.[22]

The current implementation relies on seeding sodium into the flow upstream of the test section. A salt solution is painted on the diaphragm initially separating the test and accelerator gases. When the diaphragm ruptures, a low concentration of the sodium from the salt is entrained into the flow. The sodium is detected by tuning the laser to within about 100 pm of one of the sodium D-line transitions at 589 nm. The resulting interferogram can be analyzed to visualize the sodium number density variations in the flow. The sodium density varies in proportion to the total flow density through compression and expansion. It also varies with temperature. At elevated temperatures, the sodium is thermally excited out of the ground state and eventually ionized. Because the technique detects sodium only in the ground electronic state, a fringe shift will occur in regions where either the density or temperature varies. In this study, the images were principally used to identify shock locations.

All of the images recorded in this study used finite fringe interferometry. On occasion, the fringe spacing in the freestream is nonuniform, which indicates that the seeding into the flow has not occurred uniformly. A number of interferograms show a gray area near the surface of the model, which indicates that there has been some small movement of the model between images that occurs during the recoil of the tunnel. The upstream edge of the gray area is interpreted as the position of the front of the model.

The laser system was triggered from a photosensor or an ionization gauge mounted in the accelerator tube, several meters upstream of the test section. Images were taken in the test time at around 20–30 ms after the flow started.

The regular replacement of heat transfer gauges meant that the model was removed from the test section and reinserted between shots leading to slight shot-to-shot variations in angle of attack and toroid–spacecraft distances. Alignment was achieved by observing the model through the laser system and adjusting the model until the profile indicated that it was normal to the end of the accelerator tube and normal to the laser beam. The accuracy of these measurements meant that the angle of attack, determined from comparison with the end of the accelerator tube, in most shots was 0 ± 0.5 deg.

Experimental Results and Discussion

Four measurements with the unblocked toroid and one measurement with the blocked toroid were performed at each condition. Reynolds numbers, heat fluxes, and interferograms were recorded for each condition. Random uncertainties were estimated based on fluctuations observed in the heat flux measurements. Because of occasional instrumentation problems, a number of shots were without either heat fluxes or an interferogram. The level of heat flux measured and the corresponding Stanton number were compared with theoretical values for each shot. The following sections detail the results at each condition. Sample interferograms and heat transfer traces are supplied for each, together with freestream conditions determined for the specific shot. Velocity and pressure values are measured quantities, whereas the temperature is determined from the numerical simulations. Velocity measurements are accurate to $\pm 0.2\ \mathrm{kms}^{-1}$, whereas pressures have an uncertainty of ±0.2 kPa. More complete flow calculations may be found elsewhere.[23]

Condition A: CO_2, Moderate Enthalpy

The unblocked and blocked toroids are shown in Fig. 5. In each case, the flow is from left to right with the spherical spacecraft, the mount for the spacecraft, and the toroid clearly visible. The sodium number density is visualized by the interferometry so that bends in the fringes reflect changes in the sodium ground state density, which in turn is influenced by the flow density and temperature. For the unblocked case (Fig. 5a), the locations of the shocks around the spacecraft and toroid can be seen as sharp bends in the fringes. The shock waves from the sphere and toroid are seen to interact behind the toroid, and the flow appears free of any instabilities. The slight waviness of the fringes in the freestream is indicative of nonuniform seeding of the sodium into the flow. The image for the blocked toroid (Fig. 5b) shows a significant difference from the unblocked case. The bow shock is seen to extend well out from the toroid.

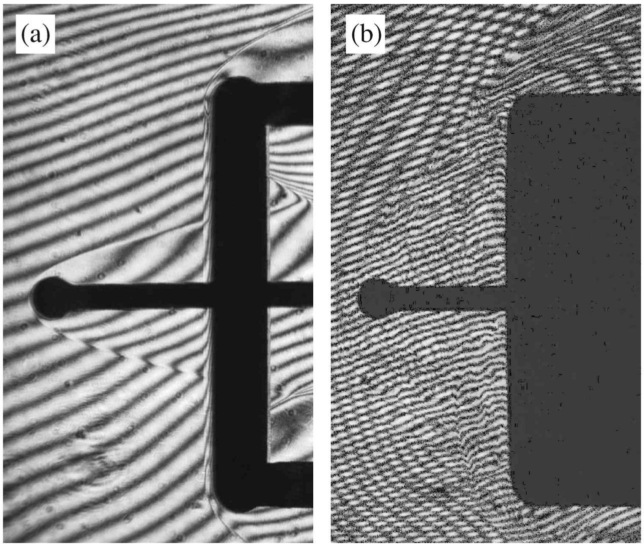

Fig. 5 Holographic interferometry images of flow condition A, flow from left to right: a) unblocked model, A1, $U_\infty = 5.5$ km/s, $p_\infty = 0.8$ kPa, and $T_\infty = 2040$ K and b) blocked model, A5, $U_\infty = 5.3$ km/s, $p_\infty = 1.0$ kPa, and $T_\infty = 2090$ K.

The crosshatch effect in this image, particularly noticeable in the freestream, results from an extra set of fringes due to the inadvertent recording of a second reference hologram. Behind the bow shock, the fringes show that the flow is highly unstable, which has resulted from the interaction of the bow shock from the blocked toroid. The differences between the two images highlight the importance of using a towed ballute that has a toroidal shape. The interaction of flow disturbances from the leading spacecraft and the ballute can then be made to take place downstream of the opening of the toroid to result in a stable flow.

Figure 6 shows sample heat transfer traces as a function of time for the unblocked and blocked toroids. For the unblocked case, a steady heat transfer level is attained soon after the arrival of the test flow at the body (set as $t = 0$ μs). The level of noise gives an indication of the uncertainty in the measurements. In contrast, the blocked toroid shows large oscillations, and, as expected, a steady level is never reached. This is indicative of the unsteadiness observed in the flow visualization. Table 2 summarizes the measured and calculated heat fluxes for all of the shots at this condition. As mentioned earlier, natural shot-to-shot variation provides a small range of freestream conditions. In general, the measured heat fluxes are below the calculated values, and this is also reflected in the Stanton numbers.

Table 2 Measured and calculated parameters for condition A

Shot	Re_e	Experiment heat flux, ±2 MW/m^2	Experiment St_e, $\pm 0.5 \times 10^{-3}$	Theory heat flux, MW/m^2	Theory St_e
A1	4990	17	4.1×10^{-3}	23.4	5.62×10^{-3}
A2	7220	12	2.2×10^{-3}	23.9	4.46×10^{-3}
A3	7220	12	2.2×10^{-3}	23.9	4.46×10^{-3}
A4	8460	——	——	24.4	4.09×10^{-3}
A5	7220	10–20	$(1.9–3.7) \times 10^{-3}$	23.9	4.46×10^{-3}

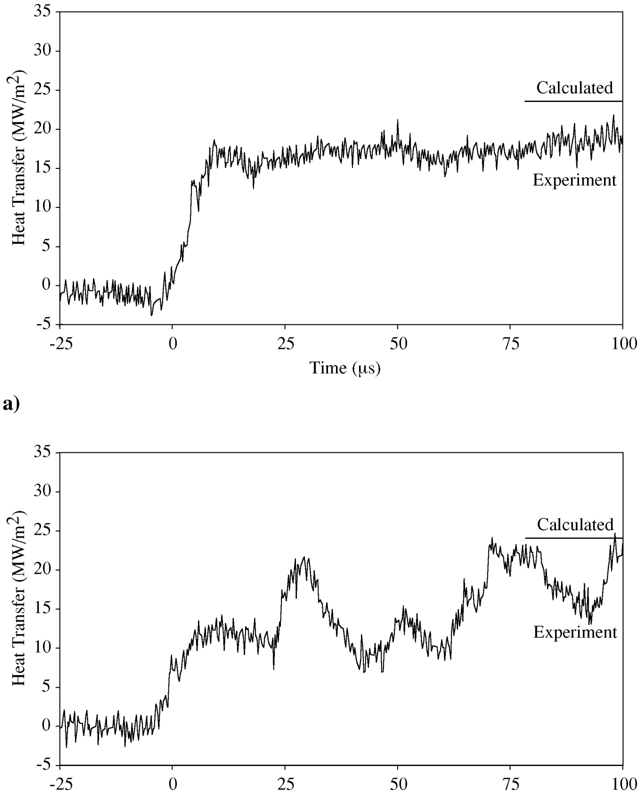

Fig. 6 Time-resolved heat transfer levels for condition A: a) unblocked model, A1, $U_\infty = 5.5$ km/s, $p_\infty = 0.8$ kPa, and $T_\infty = 2040$ K and b) blocked model, A5, $U_\infty = 5.3$ km/s, $p_\infty = 1.0$ kPa, and $T_\infty = 2090$ K.

Condition B: CO$_2$, High Enthalpy

Interferograms for this condition are shown in Fig. 7. At the higher enthalpy of condition B, the interferogram of the unblocked toroid shows that the interaction between the sphere bow shock and the shock from the toroid occurs farther downstream than the low enthalpy case. The image also shows some signs of a perturbed fringe pattern in the wake region of the body. It is unclear whether the perturbation is a result of nonuniform sodium seeding or an indication that the flowfield over the ballute is unsteady. Similar perturbations were observed in a number of images at this condition. The image for the blocked toroid again shows a high level of instability both in the bow shock and in the flow between the shock and the body.

Sample heat transfer traces are shown in Fig. 8. A much higher steady-state heat transfer level is reached than with condition A, and thus, the level of noise is comparatively smaller. A good steady level is reached for the unblocked case, but oscillations are again apparent for the blocked case. Table 3 summarizes the measured and calculated heat fluxes. In general, closer agreement is obtained between the measured and calculated heat transfer than for the moderate-enthalpy CO$_2$ case. The exception is B2, in which the freestream velocity was significantly lower than the other shots (8.8 km/s as compared to 9.4 km/s). This probably resulted from a weaker primary shock, a fact not taken into account in the calculations.

Condition C: N$_2$, Moderate Enthalpy

The low-enthalpy nitrogen tests are shown in Fig. 9. For the unblocked case, the spacecraft and toroid bow shocks are clearly defined and apparently stable. The interaction between the sphere and toroid bow shocks occurs just inside the downstream edge of the toroid, much farther upstream than for either of the carbon dioxide measurements. The blocked toroid again shows a high level of unsteadiness. (A second set of fringes is also apparent in Fig. 9.)

Figure 10 shows that the heat transfer traces are very similar to those for the moderate enthalpy carbon dioxide case: A steady level

Table 3 Measured and calculated parameters for condition B

Shot	Re_e	Experiment heat flux, ±5 MW/m^2	Experiment St_e, $\pm 0.3 \times 10^{-3}$	Theory heat flux, MW/m^2	Theory St_e
B1	3370	117	8.3×10^{-3}	101	7.22×10^{-3}
B2	6300	75	3.3×10^{-3}	109	4.77×10^{-3}
B3	3370	110	7.8×10^{-3}	101	7.22×10^{-3}
B4	3760	140	9.1×10^{-3}	106	6.92×10^{-3}
B5	3370	60	4.7×10^{-3}	101	7.22×10^{-3}

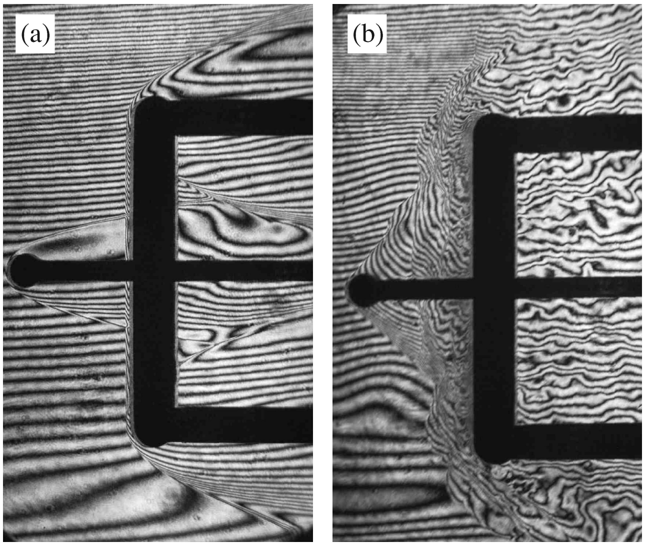

Fig. 7 Holographic interferometry images of flow condition B, flow from left to right: a) unblocked model, B4, $U_\infty = 9.3$ km/s, $p_\infty = 1.1$ kPa, and $T_\infty = 2760$ K and b) blocked model, B5, $U_\infty = 9.4$ km/s, $p_\infty = 1.1$ kPa, and $T_\infty = 2740$ K.

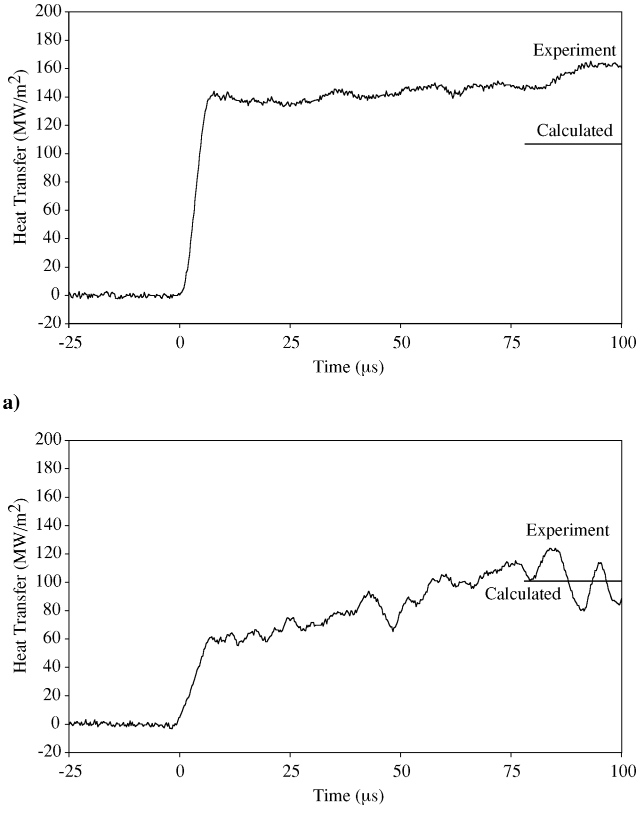

a)

b)

Fig. 8 Time-resolved heat transfer levels for condition B: a) unblocked model, B4, $U_\infty = 9.3$ km/s, $p_\infty = 1.1$ kPa, and $T_\infty = 2760$ K and b) blocked model, B5, $U_\infty = 9.4$ km/s, $p_\infty = 1.1$ kPa, and $T_\infty = 2740$ K.

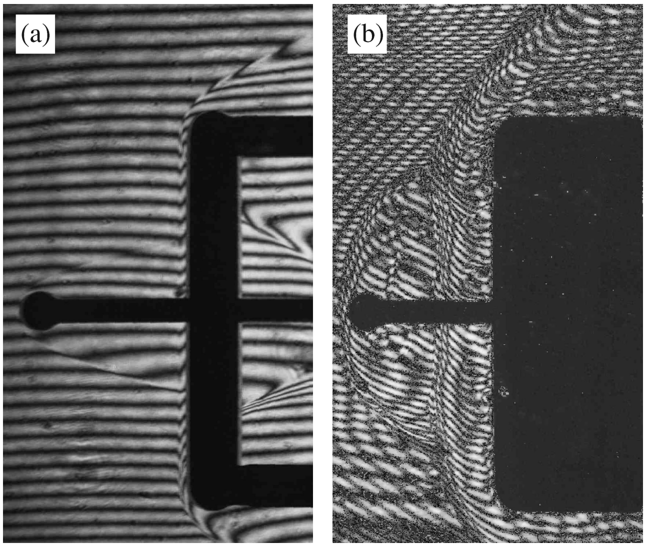

Fig. 9 Holographic interferometry images of flow condition C, flow from left to right: a) unblocked model, C2, $U_\infty = 5.7$ km/s, $p_\infty = 0.7$ kPa, and $T_\infty = 1600$ K and b) blocked model, C5, $U_\infty = 5.8$ km/s, $p_\infty = 0.6$ kPa, and $T_\infty = 1530$ K.

is obtained for the unblocked case, whereas the blocked case shows large oscillations. Table 4 summarizes the measured and calculated heat fluxes. In general, a very good agreement is obtained between experiment and theory.

Condition D: N_2, High Enthalpy

Interferograms for this condition are shown in Fig. 11. Figure 11a (unblocked) shows the shock interaction occurring well downstream of the toroid. It would appear that the optical system is not sensitive

Table 4 Measured and calculated parameters for condition C

Shot	Re_e	Experiment heat flux, ±3 MW/m²	Experiment St_e, $\pm 0.7 \times 10^{-3}$	Theory heat flux, MW/m²	Theory St_e
C1	2090	24	10×10^{-3}	24	10.1×10^{-3}
C2	2800	27	9.3×10^{-3}	26.3	9.06×10^{-3}
C3	2800	25	8.6×10^{-3}	26.3	9.06×10^{-3}
C4	2800	19	6.5×10^{-3}	26.3	9.06×10^{-3}
C5	2550	5–40	$(1.8\text{–}14.7) \times 10^{-3}$	25.5	9.36×10^{-3}

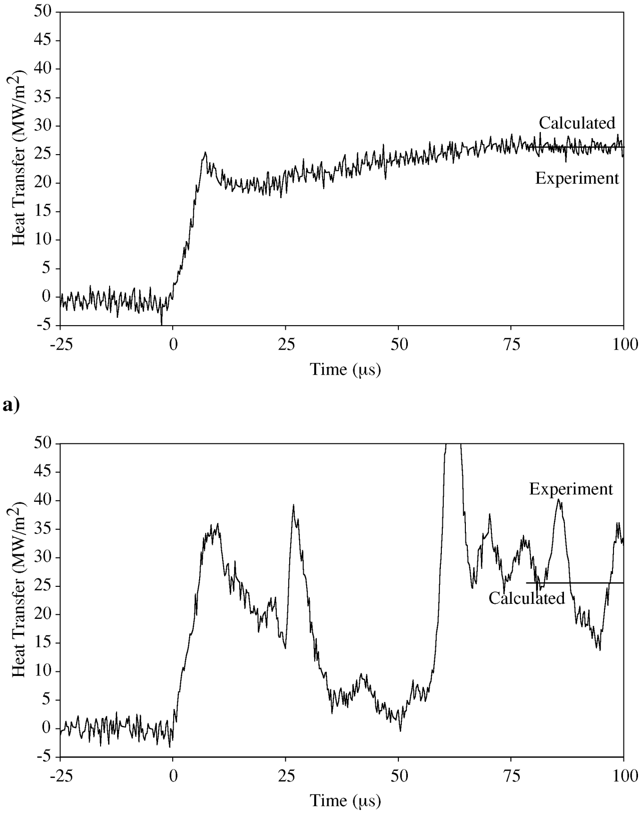

a)

b)

Fig. 10 Time-resolved heat transfer levels for condition C: a) unblocked model, C2, $U_\infty = 5.7$ km/s, $p_\infty = 0.7$ kPa, and $T_\infty = 1600$ K and b) blocked model, C5, $U_\infty = 5.8$ km/s, $p_\infty = 0.6$ kPa, and $T_\infty = 1530$ K.

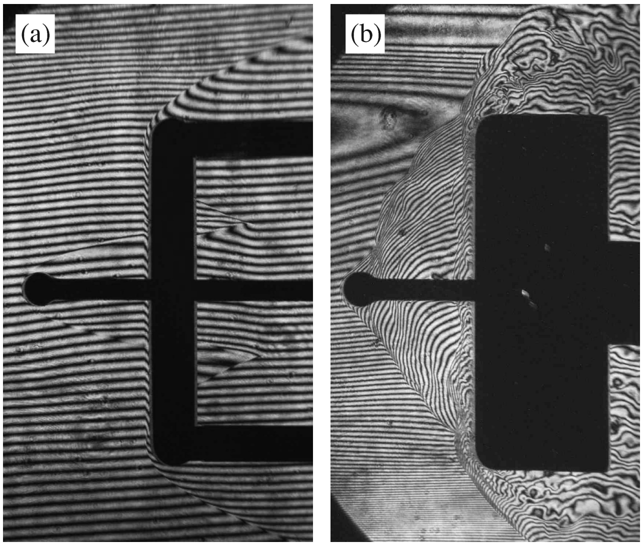

Fig. 11 Holographic interferometry images of flow condition D: flow from left to right: a) unblocked model, D3, $U_\infty = 10.0$ km/s, $p_\infty = 1.4$ kPa, and $T_\infty = 3850$ K and b) blocked model, D5, $U_\infty = 10.4$ km/s, $p_\infty = 1.1$ kPa, and $T_\infty = 3560$ K.

Table 5 Measured and calculated parameters for condition D

Shot	Re_e	Experiment heat flux, ±5 MW/m^2	Experiment St_e, $\pm 0.3 \times 10^{-3}$	Theory heat flux, MW/m^2	Theory St_e
D1	3910	——	——	125	7.02×10^{-3}
D2	4620	——	——	126	6.23×10^{-3}
D3	3610	135	8.0×10^{-3}	125	7.43×10^{-3}
D4	3610	125	7.4×10^{-3}	125	7.43×10^{-3}
D5	2640	36.7–159	$(2.8–12) \times 10^{-3}$	120	9.08×10^{-3}

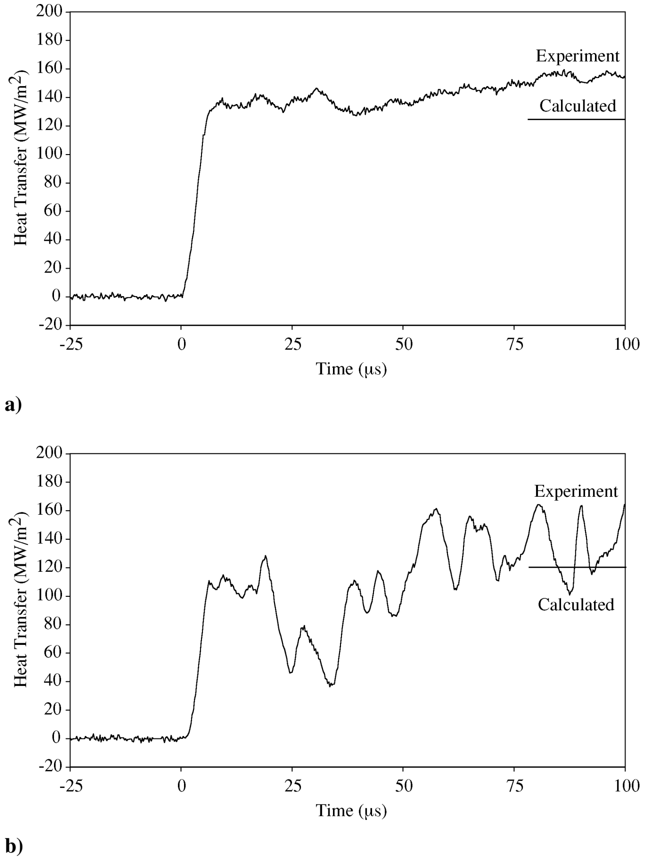

Fig. 12 **Time-resolved heat transfer levels for condition D: a) unblocked model, D3, $U_\infty = 10.0$ km/s, $p_\infty = 1.4$ kPa, and $T_\infty = 3850$ K and b) blocked model, D5, $U_\infty = 10.4$ km/s, $p_\infty = 1.1$ kPa, and $T_\infty = 3560$ K.**

to density variations downstream of the interaction because no further fringe shifts are observed despite the fact that density gradients would be expected. A possible cause is that the sodium becomes completely ionized downstream of the shock interaction due to the high temperatures involved. Some small disturbances were observed in the region downstream of the toroid between the interacting shocks and the model sting. (See discussion in preceding sections.) Major disturbances are again seen in the blocked case.

Figure 12 shows the time-resolved heat fluxes, which, as before, are steady for the unblocked case and oscillatory for the blocked case. Table 5 summarizes the measured and calculated heat fluxes. Values were not recorded for two of the shots at this condition; however, very good agreement was obtained for the other unblocked measurements. Extremely large oscillations in heat transfer levels were observed for the blocked case.

Condition E: 15% H$_2$/85% Ne, High Enthalpy

The high-enthalpy hydrogen–neon condition is shown in Fig. 13. Immediately apparent is the much larger shock standoff distance for the unblocked toroid compared to all of the other conditions, which results from a lower density jump across the shock, because real gas effects are much less important for this test gas. The shock interaction is seen to be farther upstream than both the other high enthalpy measurements. Again the flow visualization loses sensitivity downstream of the toroid.

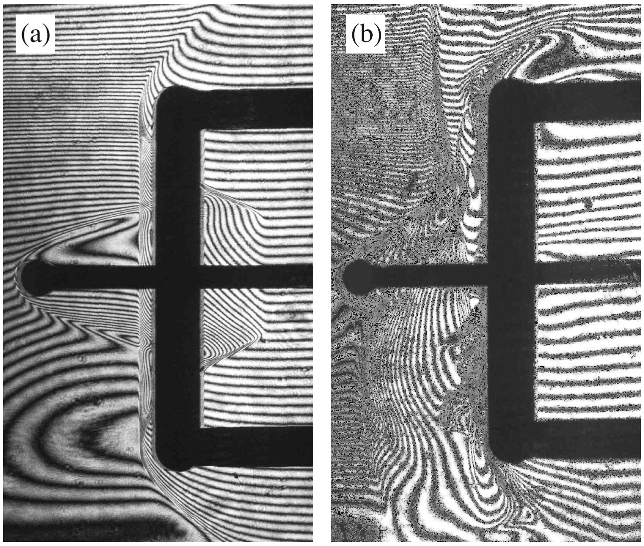

Fig. 13 **Holographic interferometry images of flow condition E, flow from left to right: a) unblocked model, E4, $U_\infty = 12.1$ km/s, $p_\infty = 1.0$ kPa, and $T_\infty = 3130$ K and b) blocked model, E5, $U_\infty = 12.1$ km/s, $p_\infty = 1.0$ kPa, and $T_\infty = 3130$ K.**

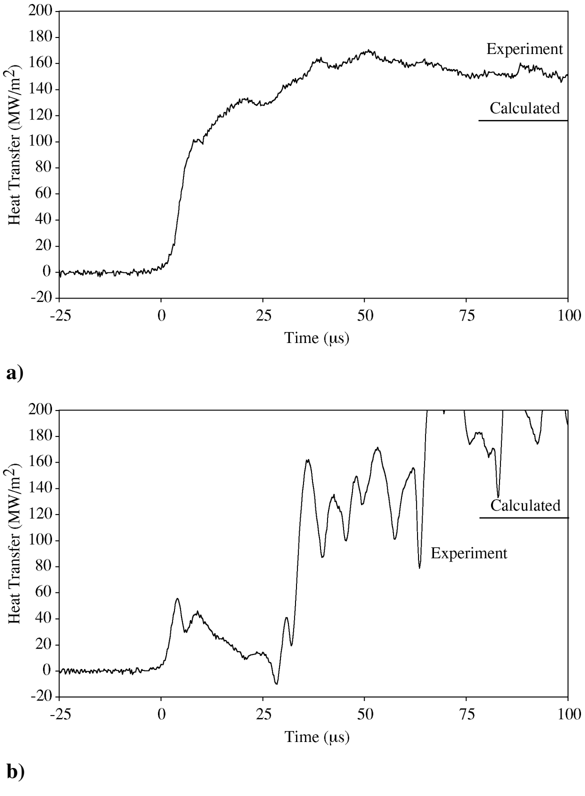

Fig. 14 **Time-resolved heat transfer levels for condition E: a) unblocked model, E1, $U_\infty = 12.2$ km/s, $p_\infty = 1.0$ kPa, and $T_\infty = 3100$ K and b) blocked model, E5, $U_\infty = 12.1$ km/s, $p_\infty = 1.0$ kPa, and $T_\infty = 3130$ K.**

Figure 14 shows sample heat fluxes, whereas Table 6 summarizes the measured and calculated heat fluxes. Heat transfer measurements at this condition generally failed to reach the steady state that was seen for most of the other conditions. Figure 14a shows a steady increase in heat flux until the peak values are reached. This may be due to the increased flow starting time necessitated by the larger shock standoff. The experimental values were taken 30 μs after shock arrival, at the end of the steady tunnel flow period. This generally yielded measured values higher than the calculated values.

Table 6 Measured and calculated parameters for condition E

Shot	Re_e	Experiment heat flux, ±20 MW/m^2	Experiment St_e, $\pm 0.3 \times 10^{-2}$	Theory heat flux, MW/m^2	Theory St_e
E1	1140	143	1.6×10^{-2}	118	1.29×10^{-2}
E2	1150	216	2.4×10^{-2}	118	1.29×10^{-2}
E3	1120	235	2.7×10^{-2}	118	1.33×10^{-2}
E4	1150	183	2.0×10^{-2}	118	1.29×10^{-2}
E5	1150	0–200	$(0\text{–}2.2) \times 10^{-2}$	118	1.29×10^{-2}

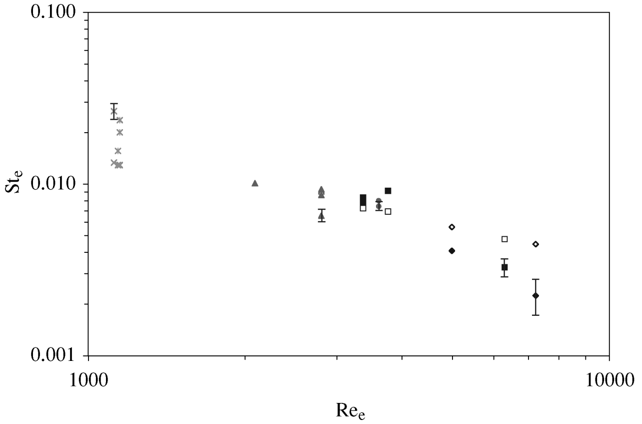

Fig. 15 Reynolds number plotted against Stanton number for all shots; typical uncertainties based on variations in the measured heat fluxes: ◆, A experiment; ◇, A theory; ■, B experiment; □, B theory; ▲, C experiment; △, C theory; ●, D experiment; ○, D theory; ⋇, E experiment; and ×, E theory.

Summary of Stanton/Reynolds Number Comparisons

The experimental and theoretical results can be represented on a plot of Reynolds number against Stanton number. Figure 15 shows such a plot for all of the operating conditions considered in this study.

The measurements and calculations show the general trend of increasing Stanton number with decreasing Reynolds number consistent with the $Re^{-1/2}$ power law as observed previously.[3] Generally good agreement between experiment and theory is observed for low Reynolds number, high Stanton number measurements. Larger discrepancies are observed where Stanton numbers are lower. Further studies are required to determine whether the cause of this lies in the measured heat transfer levels, the calculated freestream conditions, or the theoretical determination of Stanton number.

Summary of Choking Effects

The detailed process of choking is complex and is likely to involve the presence of boundary-layer and wake flows, chemical reactions, and the geometrical constrictions of the flowfield. It may also be affected by the spacecraft model support used in the experiments. For many configurations, both choked and unchoked steady solutions are possible, and the transient processes by which the flow condition is established will determine which solution is achieved. It is thought that the impulsive starting process of the experiments (with the very low prerun density in the acceleration tube) will tend to favor the unchoked condition, whereas flight at low Reynolds number in the outer atmosphere may generate a choked condition that persists as the craft descended into continuum flow. Studies are currently being conducted to investigate the effect of a lowered Reynolds number on the behavior of the flow.

The work presented here demonstrates the establishment of steady unchoked flow at sub- and superorbital speeds in an experiment. The characteristics of choked flow were investigated by physically blocking the orifice of the toroid. Such flows were seen to be fundamentally unsteady, through the evidence of flow visualization and heat transfer measurements. Additional studies on choking are reported elsewhere.[24]

Conclusions

Experiments have been successfully performed to study the flow over a spacecraft and toroidal ballute for carbon dioxide, nitrogen, and hydrogen–neon test gases. Total enthalpies ranged from 17 up to 82 MJ/kg. Heat transfer gauges provided stagnation point heat flux measurements. Holographic interferometry yielded shock shapes and standoff distances.

The images showed that the interaction of the bow shocks from the spherical spacecraft and the toroid tended to occur farther downstream at higher enthalpy, higher Mach number conditions. The flows were generally stable with the toroid configuration but were clearly unstable when the toroid was blocked. Small fringe perturbations were observed for some of the high-enthalpy unblocked conditions.

In general, heat transfer measurements showed good agreement with calculated values for the moderate- and high-enthalpy nitrogen conditions and for the high-enthalpy carbon dioxide condition. The measured values were generally lower than the calculated values for the moderate-enthalpy carbon dioxide condition. For the hydrogen–neon condition, measured heat transfer values were higher than calculated values.

Acknowledgments

This work was funded by NASA Jet Propulsion Laboratory (JPL) Contract 1227628. The guidance of Jeffrey Hall from JPL is gratefully appreciated. Computer time was supplied by the Australian Partnership for Advanced Computing facility at the Australian National University in Canberra. The input of David Griffin and Brian Loughrey from the University of Queensland Mechanical Engineering Workshop is gratefully acknowledged. Thanks also are due to Daniel Bongers for his assistance with the tunnel operation.

References

[1] Hall, J. L., "A Review of Ballute Technology for Planetary Aerocapture," International Academy of Astronautics Paper IAA-L-1112, May 2000.

[2] Hall, J. L., and Le, A. K., "Aerocapture Trajectories for Spacecraft with Large, Towed Ballutes," American Astronautical Society, AAS Paper 01-235, Feb. 2001.

[3] Rasheed, A., Fujii, K., Hornung, H. G., and Hall, J. L., "Experimental Investigation of the Flow over a Toroidal Aerocapture Ballute," AIAA Paper 2001-2460, June 2001.

[4] Stalker, R. J., and Edwards, B. P., "Hypersonic Blunt Body Flows in Hydrogen–Neon Mixtures," AIAA Paper 98-0799, Jan. 1998.

[5] Neely, A. J., and Morgan, R. G., "The Superorbital Expansion Tube Concept, Experiment and Analysis," *Aeronautical Journal*, Vol. 98, No. 973, 1994, pp. 97–105.

[6] Doolan, C. J., and Morgan, R. G., "A Two Stage Free Piston Driver," *Shock Waves*, Vol. 9, No. 4, 1999, pp. 239–248.

[7] Jacobs, P. A., "MB_CNS: A Computer Program for the Simulation of Compressible Flows," Dept. of Mechanical Engineering, Rept. 10/96, Univ. of Queensland, Brisbane, Queensland, Australia, Dec. 1996.

[8] Gordon, S., and McBride, B. J., "Computer Program for Calculation of Complex Chemical Equilibrium Compositions and Applications. I. Analysis," NASA Reference Publ. 1311, Oct. 1994.

[9] McBride, B. J., and Gordon, S., "Computer Program for Calculation of Complex Chemical Equilibrium Compositions and Applications. II. Users Manual and Program Description," NASA Reference Publ. 1311, June 1996.

[10] Macrossan, M. N., "The Equilibrium Flux Method for the Calculation of Flows with Non-Equilibrium Chemical Reactions," *Journal of Computational Physics*, Vol. 80, No. 1, 1989, pp. 204–231.

[11] Wada, Y., and Liou M. S., "A Flux Splitting Scheme with High-Resolution and Robustness for Discontinuities," AIAA Paper 94-0083, Jan. 1994.

[12] Mirels, H., "Test Time in Low-Pressure Shock Tubes," *Physics of Fluids,* Vol. 6, No. 9, 1963, pp. 1201–1214.

[13] Fay, J., and Riddell, F. R., "Theory of Stagnation Point Heat Transfer in Dissociated Air," *Journal of the Aeronautical Sciences,* Vol. 25, No. 2, 1958, pp. 73–85.

[14] Lourel, I., and Morgan, R. G., "Fast Response Coaxial Type-E Thermocouples for the Measurement of Heat Transfer in Hypersonic Facilities," Dept. of Mechanical Engineering, Rept. 2001/05, Univ. of Queensland, Brisbane, Queensland, Australia, Nov. 2001.

[15] Sanderson, S. R., "Shock Wave Interaction in Hypervelocity Flow," Ph.D. Dissertation, California Inst. of Technology, Pasadena, CA, May 1995.

[16] ASTM Committee E-20, *Manual on the Use of Thermocouples in Temperature Measurement*, 4th ed., American Society for Testing and Materials, Philadelphia, 1993.

[17] Davis, J. P., "High-Enthalpy Shock/Boundary-Layer Interaction on a Double Wedge," Ph.D. Dissertation, California Inst. of Technology, Pasadena, CA, Feb. 1999.

[18] Schultz, D., and Jones, T., "Heat Transfer Measurements in Short Duration Hypersonic Facilities," *AGARDograph* 165, Feb. 1973.

[19] Sundqvist, B., "Thermal Diffusivity and Thermal Conductivity of Chromel, Alumel, and Constantan in the Range 100–450 K," *Journal of Applied Physics*, Vol. 72, No. 2, 1992, pp. 539–545.

[20] Wegener, M. J., McIntyre, T. J., Rubinsztein-Dunlop, H., Bishop, A. I., Stalker, R. J., and Morgan, R. G., "Visualization and Analysis of Bow Shocks in a Superorbital Expansion Tube," *AIAA Journal*, Vol. 34, No. 10, 1996, pp. 2200–2202.

[21] Measures, R. M., "Spectral Line Interferometry: A Proposed Means of Selectively Measuring the Change in the Density of a Specific Atom Population," *Applied Optics*, Vol. 9, No. 3, 1970, pp. 737–741.

[22] Bishop, A. I., Littleton, B. N., McIntyre, T. J., and Rubinsztein-Dunlop, H., "Near-Resonant Holographic Interferometry of Hypersonic Flow," *Shock Waves*, Vol. 11, No. 1, 2001, pp. 23–29.

[23] McIntyre, T. J., Lourel, I., Eichmann, T. N., Morgan, R. G., Jacobs, P. A., and Bishop, A. I., "An Experimental Expansion Tube Study of the Flow over a Toroidal Ballute," Dept. of Mechanical Engineering, Rept. 2001/06, Univ. of Queensland, Brisbane, Queensland, Australia, June 2001.

[24] Lourel, I., Morgan, R. G., McIntyre, T. J., and Eichmann, T. N., "The Effect of Dissociation on Choking of Ducted Flows," AIAA Paper 2002-2894, Dec. 2002.

B. Hassan
Associate Editor

"Great Book! Loved it!"— Dr. Robert W. Farquhar, Applied Physics Laboratory

"An important book. . . I wish I had this book before starting my career!"—Dr. Enrico Lorenzini, Harvard-Smithsonian Center for Astrophysics

"I can also say that many of the tips in this book can be applied not only in the U.S. but in Europe as well."—Dipl.-Ing. (BA) Christoph Wagner, MSS, Graduate Student

ADVICE TO ROCKET SCIENTISTS: A CAREER SURVIVAL GUIDE FOR SCIENTISTS AND ENGINEERS

Jim Longuski–Purdue University

This book is a survival guide for anyone seeking a career in a high-tech field. It tells the reader not only how to survive, but how to be happy and flourish in the complex world of high-tech industries—where science and politics often clash.

Table of Contents:

Who is a Rocket Scientist? • It Doesn't Take a Rocket Scientist to be a Rocket Scientist • It's Not About Grades • Why the Work Place Is Different from School • The Golden Rule: Make your Boss Look Good • Does This Mean You Have to Kiss Butt? • What if my Boss Is Incompetent? • Check Out Your Boss Before You Accept the Job • Why You Need Two Resumes • Getting Your Resume to the Right Person • What About References? • What to Bring to the Interview • Seek out Enlightened Managers • How to Negotiate Your First Job Offer • How to Survive Your First Two Weeks on the Job • Reinvent the Wheel • What if the Rocket Doesn't Work? • How to Tell Your Boss: "We've Got a Problem." • Keep Your Boss Informed • Reality Therapy: A Few Words about the Challenger • Work on the Big Picture • How to Give a Presentation to Rocket Scientists • How to Keep Your Presentation Short and Snappy • How to Write a Technical Report • The Importance of Being Visible • How to Achieve Visibility • So You Want to Be a Professor of Rocket Science • Qualifying for the Ph.D. Program • Why Working on Your Ph.D. Is Fun • Plan Your Academic Career Early • How Will You Fund Your Research? • What Should Be on Your Academic Resume? • List the Courses You Could Teach • How Not to Give an Academic Interview • How to Prepare for an Academic Interview • The Academic Seminar for Hire • Expect a Long Wait for the Call • How to Negotiate an Academic Offer • What it Takes to Get Tenure • Train Your Graduate Students to Do Research • How to Get Promoted and Tenured at a Higher Rank • Recommended Reading

2004, 84 pages, Paperback • ISBN: 156347655X
List Price: $24.95 • **AIAA Member Price: $19.95**

AIAA American Institute of Aeronautics and Astronautics

Publications Customer Service, P.O. Box 960, Herndon, VA 20172-0960
Fax: 703/661-1501 • Phone: 800/682-2422; 703/661-1595 • E-mail: warehouse@aiaa.org
Order 24 hours a day at: www.aiaa.org

04-0431